Original Article

Assessing bone mineral density in non-weight bearing regions of the body: a texture analysis approach using abdomen and pelvis computed tomography Hounsfield units—a cross-sectional study

Min Woo Kim^, Jung Wook Huh^, Young Min Noh^, Han Eol Seo^, Dong Ha Lee^

Department of Orthopedic Surgery, Busan Medical Center, Busan, Republic of Korea

Contributions: (I) Conception and design: MW Kim, DH Lee; (II) Administrative support: JW Huh, MW Kim; (III) Provision of study materials or patients: YM Noh, DH Lee; (IV) Collection and assembly of data: HE Seo, DH Lee; (V) Data analysis and interpretation: DH Lee; (VI) Manuscript writing: All authors; (VII) Final approval of manuscript: All authors.

Correspondence to: Dong Ha Lee, MD. Department of Orthopedic Surgery, Busan Medical Center, 62, Yangjeong-ro, Busanjin-gu, Busan 47227, Republic of Korea. Email: dlee6808@gmail.com.

Background: Highlighting a gap in comprehending bone microarchitecture's intricacies using dual-energy X-ray absorptiometry (DXA), this study aims to bridge this chasm by analyzing texture in non-weight bearing regions on axial computed tomography (CT) scans. Our goal is to enrich osteoporosis patient management by enhancing bone quality and microarchitecture insights.

Methods: Conducted at Busan Medical Center from March 1, 2013, to August 30, 2022, 1,320 cases (782 patients) were screened. After applying exclusion criteria, 458 samples (296 patients) underwent bone mineral density (BMD) assessment with both CT and DXA. Regions of interest (ROIs) included spine pedicle's maximum trabecular area, sacrum Zone 1, superior/inferior pubic ramus, and femur's greater/lesser trochanters. Texture features (n=45) were extracted from ROIs using gray-level co-occurrence matrices. A regression model predicted BMD, spotlighting the top five influential texture features.

Results: Correlation coefficients ranged from 0.709 (lowest for total femur BMD) to 0.804 (highest for femur intertrochanter BMD). Mean squared error (MSE) values were also provided for lumbar and femur BMD/bone mineral content (BMC) metrics. The most influential texture features included contrast_32, correlation_32_v, and three other metrics.

Conclusions: By melding traditional DXA and CT texture analysis, our approach presents a comprehensive bone health perspective, potentially revolutionizing osteoporosis diagnostics.

Keywords: Texture analysis; non-weight bearing regions of interest (non-weight bearing ROIs); bone microarchitecture; bone mineral density (BMD); quantitative techniques

---

^ ORCID: Min Woo Kim, 0000-0001-5609-3507; Jung Wook Huh, 0000-0001-9216-8238; Young Min Noh, 0000-0001-7149-7526; Han Eol Seo, 0000-0002-1053-0764; Dong Ha Lee, 0000-0001-7826-2148.

Introduction

The assessment of bone quality and microarchitecture plays a critical role in determining bone strength and fracture risk. Conventionally, the dual-energy X-ray absorptiometry (DXA) and quantitative computed tomography (QCT) have been employed for such evaluations. DXA is extensively used to measure bone mineral density (BMD) and serves as the gold standard for diagnosing osteoporosis (1). Meanwhile, QCT utilizes computed tomography (CT) imaging to quantify BMD and other bone parameters, frequently used to evaluate bone health and fracture risk, particularly in patients with osteoporosis (2,3).

Despite their extensive use, DXA and QCT have inherent limitations, which has led to the exploration of supplementary techniques such as CT texture analysis (4,5). This technique assesses bone quality and microarchitecture by examining variations in pixel intensity and spatial distribution on CT images. By providing an additional layer of information about fracture risk beyond DXA BMD measurements alone, CT texture analysis has shown its potential in clinical applications. It can detect subtle changes in bone microarchitecture, such as trabecular spacing and connectivity, which may not be reflected in BMD measurements. Furthermore, it can identify patients at risk for fractures, even if their BMD is within the normal range, by revealing changes in bone microarchitecture that may signify reduced bone strength (6).

One significant advantage of CT texture analysis lies in its potential to reduce additional radiation exposure and enhance patient comfort (4). Often, CT scans are conducted for various clinical reasons, and conducting a CT texture analysis on these already acquired images doesn't necessitate additional radiation exposure (5,6). While CT texture analysis offers the advantage of potentially reducing radiation exposure, it's important to recognize its limitations, such as the dependence on image quality, potential variations based on scanning protocols, and the need for robust software algorithms. However, even with these constraints, the method's potential to reduce radiation risk underscores its value as a safer approach for patients.

Notable studies (7,8) have demonstrated the predictive power of CT texture analysis in assessing fracture risk. They found a significant association between various texture analysis parameters and fracture risk, even after accounting for variables like age, body mass index (BMI), and DXA BMD.
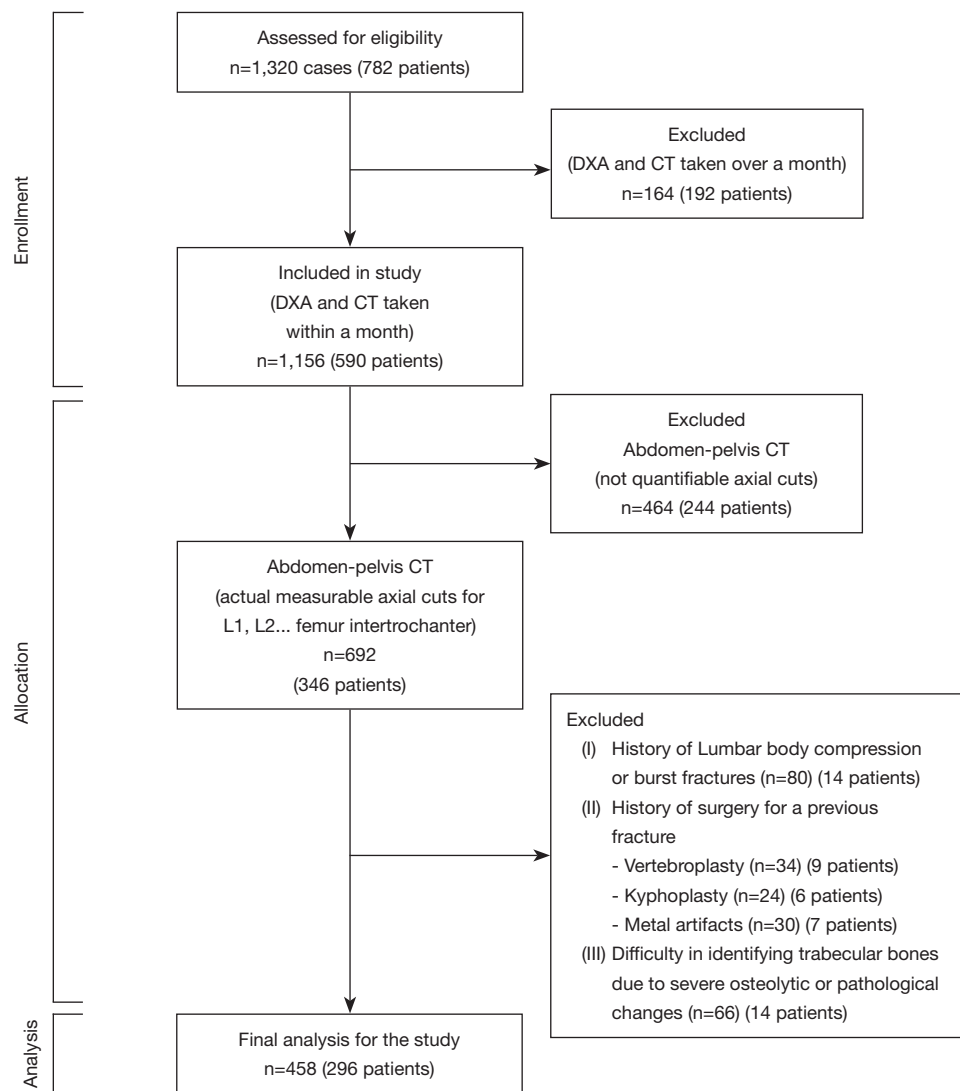
However, the application of CT texture analysis for evaluating bone quality and microarchitecture in non-weight bearing regions remains underexplored. Such regions of interest (ROIs) on axial CT scans typically include the lumbar spine and hip, promising areas for assessing bone health when combined with DXA BMD measurements (1,9-11). For example, texture analysis of the spine pedicle, Zone 1 of the sacrum, superior and inferior pubic ramus bones, and the greater and lesser trochanters of the femur, has offered valuable insights about bone quality and fracture risk prediction (12).

Despite the potential advantages, the number of studies investigating CT texture analysis in non-weight bearing regions is limited (7,13,14). This underlines the need for more focused research on this promising technique. Expanding the application of CT texture analysis to non-weight bearing regions could broaden our understanding of bone health and, in turn, lead to more effective treatment decisions for patients at risk of osteoporotic fractures.

Overall, texture analysis of non-weight bearing ROIs on axial CT scans offers a promising technique for evaluating bone quality and assessing fracture risk. This approach can provide valuable information about bone microarchitecture in a variety of anatomical regions, including the spine and femur, which is not entirely captured by DXA BMD measurements (15). When used in conjunction with DXA BMD, texture analysis has the potential to not only deepen our understanding of bone health but also improve our ability to predict fracture risk. This could enable more informed treatment decisions for patients at risk of osteoporotic fractures or for those suffering from other bone-related conditions.

Objective

In this study, we set two objectives. The primary objective is to assess the potential of texture analysis of non-weight bearing ROIs on axial CT scans to provide complementary information about bone quality and microarchitecture. The secondary objective is to explore how this data can aid in predicting fracture risk and guiding treatment decisions in patients with osteoporosis or other bone-related conditions. We present this article in accordance with the STROBE reporting checklist (available at https://qims.amegroups.com/article/view/10.21037/qims-23-512/rc).

7486

Kim et al. CT texture analysis for bone density assessment

Figure 1 Diagram illustrating the process of case selection. DXA, dual-energy X-ray absorptiometry; CT, computed tomography.

Methods

Participant recruitment

In this cross-sectional study conducted at Busan Medical Center, we retrospectively analyzed 1,156 cases involving 590 patients who had undergone both CT and DXA scans from March 1, 2013, to August 30, 2022. Our study included patients who fulfilled the following criteria. Firstly, the time interval between their CT and DXA scans had to be less than one month. This was to ensure consistency in the bone conditions captured in both scans, thereby allowing for an accurate comparison and analysis. Secondly, the CT scans had to cover specific regions, particularly the

abdomen and pelvis. Notably, the axial cuts of the scans should clearly show the L1–S1 vertebral body and pedicle. In addition, the axial cuts should cover both the right and left superior and inferior pubic ramus, as well as the femur's greater and lesser trochanters. These areas were critically analyzed in our texture analysis approach for assessing BMD. Patients were excluded if they had a history of previous fractures, previous surgery for a fracture, severe osteolytic changes, or metal artifacts. After applying the exclusion criteria, the analysis was performed on 458 sets of ROIs obtained from axial CT scans of 296 patients, as shown in *Figure 1*. The study was conducted in accordance with the Declaration of Helsinki (as revised in 2013).

This study was approved by the Busan Medical Center Institutional Review Board (IRB No. 2023-01-002) and individual consent for this retrospective analysis was waived.

Abdomen-pelvis CT imaging protocols

The CT imaging was carried out on a Siemens SOMATOM 128, Definition AS+ scanner (manufactured by Siemens Healthcare, Forchheim, Germany) using a single-energy CT protocol. The following parameters were utilized during the imaging: 120 kVp, 247 mA, dose modulation, 0.6-mm collimation, and an effective pitch of 0.8. The acquired images had a 3.0 mm slice thickness for both the abdomen and pelvis CT, with a 3.0 mm slice increment.

DXA imaging protocols

At our institution, BMD values were predominantly determined using DXA as the reference standard. The clinical assessment procedure specifically involved conducting DXA measurements on the L1–L4 regions of the spine and the neck and intertrochanteric areas of the femur using a GE Lunar Prodigy DXA device (manufactured by GE Healthcare, Chicago, USA) following a well-defined imaging protocol (16). The obtained BMD values from these DXA images were automatically analyzed and reports were subsequently generated using the Physicians Report Writer DX software provided by the vendor, Hologic (located in Discovery, WI, USA).

ROIs of non-weight bearing portions of body

In order to perform statistical analysis of the bone images, the researchers limited their selection of ROIs to the cancellous bone, avoiding the cortical bone that could introduce inaccuracies due to its differing structure and density. To define these ROIs, the thresholding method was selected from various available options (17). For each patient, a 2D slice image was chosen from the CT scans that contained the largest cancellous bone area in the lumbar body, ilium, and proximal femur regions. Based on the methodology employed by Link (18), a rectangular region was selected as it covers a comprehensive extent of the trabecular area, thus yielding more representative texture analysis results. This region was utilized for texture analysis, as depicted in *Figure 2*.

Process of obtaining 45 features

The study used a total of 45 features extracted from ROIs, including five intensity-based features and 40 texture-based features. The intensity-based features were obtained from the ROI image histogram and provided information about bone intensities. The gray-level co-occurrence matrix (GLCM) is a statistical method that examines the texture of an image by calculating how often pairs of pixel with specific values and in a specified spatial relationship occur in an image (19). This matrix is instrumental in gauging various properties of the texture of an image, making it a valuable tool in medical imaging studies.

The 40 texture-based features in our study were extracted using a GLCM matrix. This matrix provides crucial information about the spatial relationships between adjacent pixels across a 2D image. The foundation of the GLCM lies in its capacity to measure the frequency of pairs of pixel values (i.e., gray levels) at a given offset. The GLCM was derived from a matrix size of N × N. For our analysis, eight separate GLCMs were created for each sample ROI image. These matrices served to measure five primary statistics—entropy, contrast, correlation, homogeneity, and variance. Each of these statistics was evaluated across four distinct levels (N=16, 32, 64, 128) and in two orientations (horizontal and vertical). The essence of these measures is to capture the intricacies and patterns of bone structures that might not be evident through mere visual inspection.

Combining both intensity-based and texture-based features, we then utilized them as input for a Linear Regression (LR) model to provide a robust estimation of BMD.

Statistical analysis

All statistical analyses were undertaken using MATLAB 9.10 R2021a (MathWorks, Natick, Massachusetts, USA). A multiple regression model was deployed to examine the relationship between estimated BMD values derived from texture features and reference BMD values acquired via DXA.

For the purpose of this analysis, each feature was designated as x_{ij}, wherein 'i' symbolizes the feature index and 'j' marks the specific sample or case under consideration. To ensure consistency and minimize the influence of outliers, these features underwent normalization using their
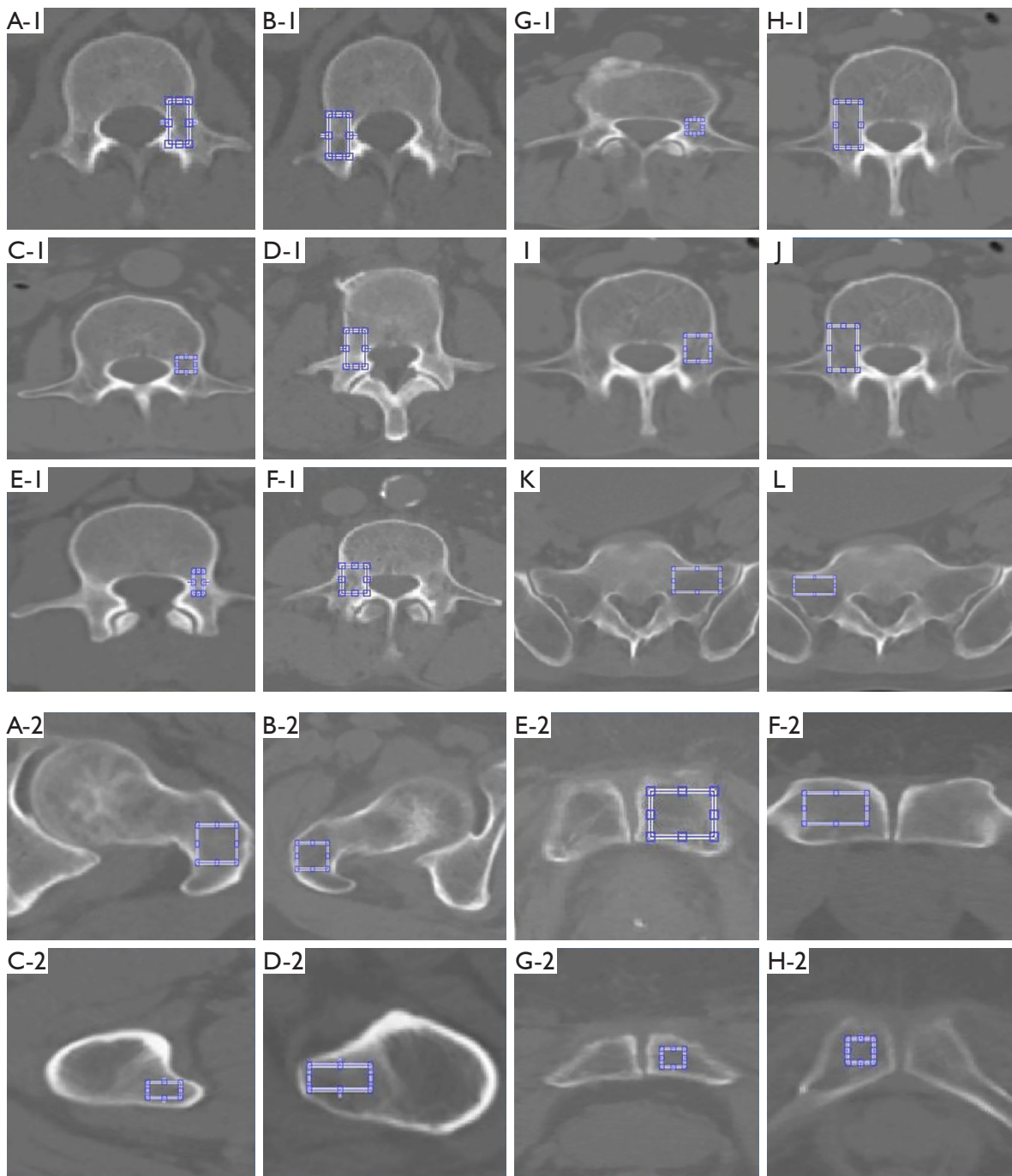
Figure 2 Areas of interest in cross-sectional abdominal-pelvic CT scans. (A-1) Lumbar 1 left pedicle, (B-1) lumbar 1 right pedicle, (C-1) lumbar 2 left pedicle, (D-1) lumbar 2 right pedicle, (E-1) lumbar 3 left pedicle, (F-1) lumbar 3 right pedicle, (G-1) lumbar 4 left pedicle, (H-1) lumbar 4 right pedicle, (I) lumbar 5 left pedicle, (J) lumbar 5 right pedicle, (K) sacrum Zone 1 left pedicle, (L) sacrum Zone 1 right pedicle. (A-2) Femur left greater trochanter, (B-2) femur right greater trochanter, (C-2) femur left lesser trochanter, (D-2) femur right lesser trochanter, (E-2) pelvis left superior pubic ramus, (F-2) pelvis right superior pubic ramus, (G-2) pelvis left inferior pubic ramus, (H-2) pelvis right inferior pubic ramus. The blue line demarcates the ROIs specific to the non-weight bearing portions of the body, emphasizing the cancellous bone and avoiding the cortical bone. These regions were defined using a thresholding method as per the referenced techniques (13). CT, computed tomography; ROI, region of interest.

Table 1 The LR model's CC and MSE

Datasets	CC, 45 values	MSE, 45 values
Total lumbar BMD	0.726	0.125
Total lumbar BMC	0.720	11.243
Total femur BMD	0.709	0.131
Total femur BMC	0.719	5.02
Femur neck BMD	0.721	0.143
Femur neck BMC	0.711	0.572
Femur intertrochanter BMD	0.804	0.129
Femur intertrochanter BMC	0.729	3.91

LR, Linear Regression; MSE, mean squared error; CC, correlation coefficient; BMD, bone mineral density; BMC, bone mineral content.

respective sample mean (xi) and standard deviation (σi). In tandem, the reference BMD values, represented by yj, were normalized drawing on the sample mean (y) and its standard deviation (σ).

Our chosen LR model employed a weighted aggregation of 45 distinct features, augmented by a singular bias term, to predict BMD estimates. The following equation provides a mathematical representation of our model:

$$yj = w0 + \sum wi \times xij \qquad [1]$$

Here, the objective was to optimize the weights (wi) to narrow down the discrepancy between the projected BMD values and their actual counterparts present in our dataset. The magnitude of this deviation was quantified by the formula:

$$e = \sum \left(yj - \hat{yj} \right) 2 \qquad [2]$$

It's pertinent to mention that our study deliberately refrained from implementing regularization techniques and dividing the dataset into training and test subsets, thus sidestepping potential pitfalls of bias and overfitting.

BMD correlation's maximum index based on five features

In our analysis, we identified five key features that demonstrated the highest correlation with BMD values. The correlation for each feature was determined using Pearson's correlation coefficient. This process was iteratively conducted for each feature index, ranging from 1 to 45. The correlation for each feature was calculated with

respect to BMD across all femur variants in the dataset, which included LumbarL-1, PelvisSupR-1, among others. This comprehensive examination led to the identification of the five features showing the maximum correlation indices with BMD.

Results

Demographic information of the patients

This study involved a total of 296 patients, composed of 122 males and 174 females. The average age of the patients was 58.21±11.88 years. We analyzed the data obtained from the patients' CT and DXA scans, with a mean gap of 2.51±3.52 days between the two procedures. The average BMI for the male patients was 24.55±3.80 kg/m^2, and for female patients, it was 22.91±5.30 kg/m^2.

Statistical test for measuring the association between variables

Our study involved the generation of scatter plots (Appendix 1, Figures S1-S8) that juxtapose predicted BMD values and actual BMD values for all cases. In our study, the neural network model utilized was inspired by the deep learning principles described by Kriegeskorte and Golan [2019] (13). This model, comprised of interconnected nodes spread across multiple layers, excels in deciphering intricate patterns in data. After training the model on our dataset, its predictive accuracy was showcased in the graphs provided. In *Table 1*, we encapsulate the statistical analysis, showcasing both the correlation coefficient and the mean squared error (MSE) for the predicted versus reference BMD values.

Applying a LR model (15), we examined datasets with varying BMD and bone mineral content (BMC) parameters derived from different parts of the femur and lumbar region. The obtained correlation coefficients and MSE values demonstrate the prediction accuracy of our model: 0.726 (0.125) for total lumbar BMD, 0.720 (11.243) for total lumbar BMC, 0.709 (0.131) for total femur BMD, 0.719 (5.02) for total femur BMC, 0.721 (0.143) for femur neck BMD, 0.711 (0.572) for femur neck BMC, 0.804 (0.129) for femur intertrochanter BMD, and 0.729 (3.91) for femur intertrochanter BMC.

In *Table 1*, we also compare the performance of our method (employing 45 features) with a conventional approach that only uses the mean Hounsfield unit (HU) feature. Evidently, our LR model, which utilizes all

45 features, offers significantly enhanced precision in estimating the average attenuation coefficient.

In the referenced figures (Appendix 1, Figures S1-S8), each scatter plot illustrates the correlation between predicted and actual BMD values, with the degree of dispersion around the line of best fit representing the accuracy of our model. Lower dispersion indicates better prediction accuracy.

Maximum 5 index correlation of BMD estimates

The five features that demonstrated the highest correlation with BMD estimates were labeled as 6, 12, 22, 26, and 42. The corresponding Pearson correlation coefficients for these features represent different texture parameters derived from the CT images, specifically, "contrast_32", "correlation_32_v", "correlation_64_v", "correlation_128_v", and "correlation_256_v", respectively (as illustrated in *Figure 3*). In the context of our study, these labels are names assigned to the different texture parameters, where the number denotes the size of the neighborhood considered for texture calculation and the prefix denotes the texture feature (contrast or correlation). These findings underscore the potential significance of these specific features in elucidating the relationship between bone texture and BMD, which could have important implications for the diagnosis and management of bone disorders.

Discussion

Our study incorporated CT HU texture analysis with 45 features to estimate BMD. The resultant correlation coefficients for our eight BMD/BMC targets, including Total Lumbar BMD and Femur Intertrochanter BMC, ranged from 0.709 to 0.804. This range underscores a moderate to strong positive correlation between the predicted BMD values and the established BMD measurements (20).

The superior average attenuation coefficient scores of our LR model, compared to traditional methods that use the mean HU feature, illustrate the method's enhanced performance (4,8). This suggests that our approach could potentially provide a deeper, more accurate insight into bone health. Our analysis pinpointed five key features with strong correlation to BMD estimates, specifically labeled as 6, 12, 22, 26, and 42. These represent texture parameters from CT images, such as "contrast_32" and various "correlation" metrics, as shown in *Figure 3*. Drawing from prior research, such texture attributes, including contrast and autocorrelation, stand out in medical image analysis,

although the relevance of features can vary based on the imaging technique and research focus (5,21).

Distinctively, our study went beyond traditional research, which mainly emphasized weight-bearing regions. We expanded our analysis to include non-weight bearing regions, ensuring a holistic interpretation of bone health, an aspect previously underrepresented.

BMD, as valuable as it is, might not capture the entire essence of bone health (22). Hence, our method, which compared BMD with non-weight bearing ROI on CT scans using texture analysis, is meant to complement, not replace, traditional BMD measurements. It brings to light additional aspects of bone health, particularly the bone's microarchitecture, which plays a pivotal role in fracture risk assessment (7,23,24).

Our approach, which melds the traditional DXA BMD and our innovative CT texture analysis, offers a dual perspective on bone health (25). While DXA BMD continues to be the cornerstone for assessing BMC and density, the texture analysis method offers a deeper dive into the intricate microstructural details of the bone, giving practitioners a more robust diagnostic tool.

We recognize that our study's manual selection of the trabecular bone might introduce some subjectivity, potentially impacting the consistency of results across samples. The variance in our recorded MSE values, from as low as 0.129 for femur neck BMD to as high as 11.243 for total lumbar BMC, further underlines this.

While our study contributes valuable insights into estimating BMD using CT texture analysis (1,21,26), it does present certain limitations. A potential limitation is the manual selection of only the trabecular bone for analysis, which introduces the possibility for error. Although the "rectangular region" indicated in the methods was used for this selection, there is still potential for subjectivity and variation in the selection process, which might impact the accuracy of the results. We acknowledge this limitation and have strived to mitigate it through rigorous methodology and consistency in the selection process (27,28). Additionally, juxtaposing our results with QCT-derived BMD measures could solidify the validity and applicability of our approach.

We understand that BMD measurements are traditionally taken at weight-bearing sites like the hip and spine. Still, our study argues that non-weight bearing ROIs are also essential for evaluation, as they can be affected by conditions such as osteoporosis and osteopenia (1,7,29). Texture analysis of these non-weight bearing ROIs might be more
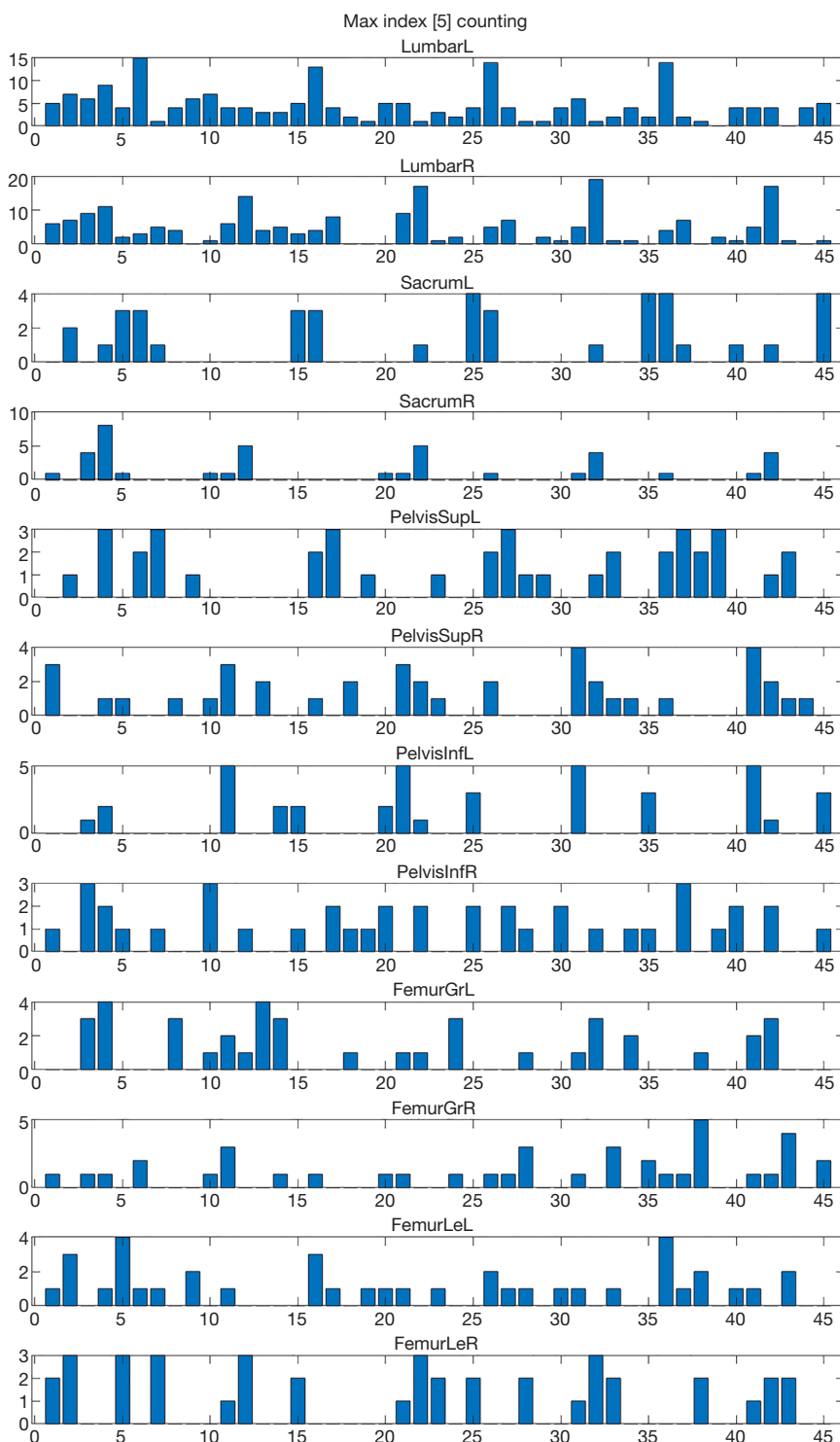
Figure 3 Max index [5] counting for BMD correlation—this figure represents the highest index [5] value obtained for BMD correlation. The individual alphabetic markers correspond to various measurement regions as follows: LumbarL, lumbar left; LumbarR, lumbar right; SacrumL, sacrum left; SacrumR, sacrum right; PelvisSupL, pelvis superior ramus left; PelvisSupR, pelvis superior ramus right; PelvisInfL, pelvis inferior ramus left; PelvisInfR, pelvis inferior ramus right; FemurGrL, femur greater trochanter left; FemurGrR, femur greater trochanter right; FemurLeL, femur lesser trochanter left; FemurLeR, femur lesser trochanter right. BMD, bone mineral density.

sensitive to changes in bone quality and microarchitecture occurring earlier in the disease process compared to BMD measurements.

Conclusions

Our study, rooted in integrating the traditional DXA BMD measures and the contemporary CT texture analysis, offers a fresh lens through which to view and diagnose bone health. This integrated approach, we believe, can reshape the landscape of osteoporosis diagnostics and treatments, providing both practitioners and patients with a more holistic understanding of bone health.

Acknowledgments

Footnote

Reporting Checklist: The authors have completed the STROBE reporting checklist. Available at https://qims.amegroups.com/article/view/10.21037/qims-23-512/rc

Conflicts of Interest: All authors have completed the ICMJE uniform disclosure form (available at https://qims.amegroups.com/article/view/10.21037/qims-23-512/coif). The authors have no conflicts of interest to declare.

Ethical Statement: The authors are accountable for all aspects of the work in ensuring that questions related to the accuracy or integrity of any part of the work are appropriately investigated and resolved. The study was conducted in accordance with the Declaration of Helsinki (as revised in 2013). This study was approved by the Busan Medical Center Institutional Review Board (IRB No. 2023-01-002) and individual consent for this retrospective analysis was waived.

References

1. Holubiac IŞ, Leuciuc FV, Crăciun DM, Dobrescu T. Effect of Strength Training Protocol on Bone Mineral Density for Postmenopausal Women with Osteopenia/Osteoporosis Assessed by Dual-Energy X-ray Absorptiometry (DEXA). Sensors (Basel) 2022;22:1904.
2. Kim GU, Park WT, Chang MC, Lee GW. Diagnostic Technology for Spine Pathology. Asian Spine J 2022;16:764-75.
3. Niu X, Huang Y, Li X, Yan W, Lu X, Jia X, Li J, Hu J, Sun T, Jing W, Guo J. Development and validation of a fully automated system using deep learning for opportunistic osteoporosis screening using low-dose computed tomography scans. Quant Imaging Med Surg 2023;13:5294-305.
4. Corrias G, Micheletti G, Barberini L, Suri JS, Saba L. Texture analysis imaging "what a clinical radiologist needs to know". Eur J Radiol 2022;146:110055.
5. Materka A. Texture analysis methodologies for magnetic resonance imaging. Dialogues Clin Neurosci 2004;6:243-50.
6. Tokeshi S, Eguchi Y, Suzuki M, Yamanaka H, Tamai H, Orita S, Inage K, Shiga Y, Hagiwara S, Nakamura J, Akazawa T, Takahashi H, Ohtori S. Relationship between Skeletal Muscle Mass, Bone Mineral Density, and Trabecular Bone Score in Osteoporotic Vertebral Compression Fractures. Asian Spine J 2021;15:365-72.
7. Sollmann N, Kirschke JS, Kronthaler S, Boehm C, Dieckmeyer M, Vogele D, Kloth C, Lisson CG, Carballido-Gamio J, Link TM, Karampinos DC, Karuppasamy S, Beer M, Krug R, Baum T. editors. Imaging of the Osteoporotic Spine – Quantitative Approaches in Diagnostics and for the Prediction of the Individual Fracture Risk. Rofo 2022;194:1088-99.
8. Dieckmeyer M, Sollmann N, El Husseini M, Sekuboyina A, Löffler MT, Zimmer C, Kirschke JS, Subburaj K, Baum T. Gender-, Age- and Region-Specific Characterization of Vertebral Bone Microstructure Through Automated Segmentation and 3D Texture Analysis of Routine Abdominal CT. Front Endocrinol (Lausanne) 2021;12:792760.
9. Seo M, Choi MH, Lee YJ, Jung SE, Rha SE. Evaluating the added benefit of CT texture analysis on conventional CT analysis to differentiate benign ovarian cysts. Diagn Interv Radiol 2021;27:460-8.
10. Pickhardt PJ. Value-added Opportunistic CT Screening: State of the Art. Radiology 2022;303:241-54.

11. Zhu Z, Zhao Y, Zhao X, Wang X, Yu W, Hu M, Zhang X, Zhou C. Impact of preset and postset adaptive statistical iterative reconstruction-V on image quality in nonenhanced abdominal-pelvic CT on wide-detector revolution CT. Quant Imaging Med Surg 2021;11:264-75.

12. Pennington Z, Ehresman J, Lubelski D, Cottrill E, Schilling A, Ahmed AK, Feghali J, Witham TF, Sciubba DM. Assessing underlying bone quality in spine surgery patients: a narrative review of dual-energy X-ray absorptiometry (DXA) and alternatives. Spine J 2021;21:321-31.

13. Kriegeskorte N, Golan T. Neural network models and deep learning. Curr Biol 2019;29:R231-6.

14. Zhang B, Yu K, Ning Z, Wang K, Dong Y, Liu X, et al. Deep learning of lumbar spine X-ray for osteopenia and osteoporosis screening: A multicenter retrospective cohort study. Bone 2020;140:115561.

15. Guo B, Cai Q, Mai J, Hou L, Zeng C, Gan J, Tan Z, Li Y, Cheng Y, Shang J, Tang Y, Ling X, Gong J, Wang L, Xu H. The precision study of dual energy X-ray absorptiometry for bone mineral density and body composition measurements in female cynomolgus monkeys. Quant Imaging Med Surg 2022;12:2051-7.

16. Shepherd JA, Fan B, Lu Y, Wu XP, Wacker WK, Ergun DL, Levine MA. A multinational study to develop universal standardization of whole-body bone density and composition using GE Healthcare Lunar and Hologic DXA systems. J Bone Miner Res 2012;27:2208-16.

17. Wang Y, Chen H, Heng Q, Hou W, Fan Y, Wu Z, Wang J, Savvides M, Shinozaki T, Raj B, Schiele B, Xie X. Freematch: Self-adaptive thresholding for semi-supervised learning. arXiv 2022. arXiv:2205.07246.

18. Link TM. Osteoporosis imaging: state of the art and advanced imaging. Radiology 2012;263:3-17.

19. Aggarwal AK. Learning texture features from GLCM for classification of brain tumor MRI images using random forest classifier. WSEAS Transactions on Signal Processing 2022;18:60-3.

20. Akoglu H. User's guide to correlation coefficients. Turk J Emerg Med 2018;18:91-3.

21. Therkildsen J, Winther S, Nissen L, Jørgensen HS, Thygesen J, Ivarsen P, Frost L, Langdahl BL, Hauge EM, Böttcher M. Feasibility of Opportunistic Screening for Low Thoracic Bone Mineral Density in Patients Referred for Routine Cardiac CT. J Clin Densitom 2020;23:117-27.

22. Yano Y, Iwata E, Sada T, Ueno Y, Hyakuda Y, Kawasaki S, Okuda A, Shigematsu H, Uematsu K, Yajima H, Tanaka Y. Preliminary Screening Method for Low Bone Mineral Density Using a Self-Reported Questionnaire among Peri- and Postmenopausal Women. Asian Spine J 2022;16:927-33.

23. McCloskey EV, Odén A, Harvey NC, Leslie WD, Hans D, Johansson H, et al. A Meta-Analysis of Trabecular Bone Score in Fracture Risk Prediction and Its Relationship to FRAX. J Bone Miner Res 2016;31:940-8.

24. Jang HD, Kim EH, Lee JC, Choi SW, Kim HS, Cha JS, Shin BJ. Management of Osteoporotic Vertebral Fracture: Review Update 2022. Asian Spine J 2022;16:934-46.

25. Pickhardt PJ, Lee LJ, del Rio AM, Lauder T, Bruce RJ, Summers RM, Pooler BD, Binkley N. Simultaneous screening for osteoporosis at CT colonography: bone mineral density assessment using MDCT attenuation techniques compared with the DXA reference standard. J Bone Miner Res 2011;26:2194-203.

26. Choi ES, Shin HD, Sim JA, Na YG, Choi WJ, Shin DD, Baik JM. Relationship of Bone Mineral Density and Knee Osteoarthritis (Kellgren-Lawrence Grade): Fifth Korea National Health and Nutrition Examination Survey. Clin Orthop Surg 2021;13:60-6.

27. Castellanos NP, Martínez E, Gutierrez J. Improving osteoporosis diagnosis in children using image texture analysis. Annu Int Conf IEEE Eng Med Biol Soc 2011;2011:6184-7.

28. Ollivier M, Le Corroller T, Blanc G, Parratte S, Champsaur P, Chabrand P, Argenson JN. Radiographic bone texture analysis is correlated with 3D microarchitecture in the femoral head, and improves the estimation of the femoral neck fracture risk when combined with bone mineral density. Eur J Radiol 2013;82:1494-8.

29. Boutin RD, Lenchik L. Value-Added Opportunistic CT: Insights Into Osteoporosis and Sarcopenia. AJR Am J Roentgenol 2020;215:582-94.

Appendix 1 Supplementary materials for the Results section

Results

Statistical test for measuring the association between variables

In the referenced figures (*Figures S1-S8*), each scatter plot illustrates the correlation between predicted and actual BMD values, with the degree of dispersion around the line of best fit representing the accuracy of our model. Lower dispersion indicates better prediction accuracy.
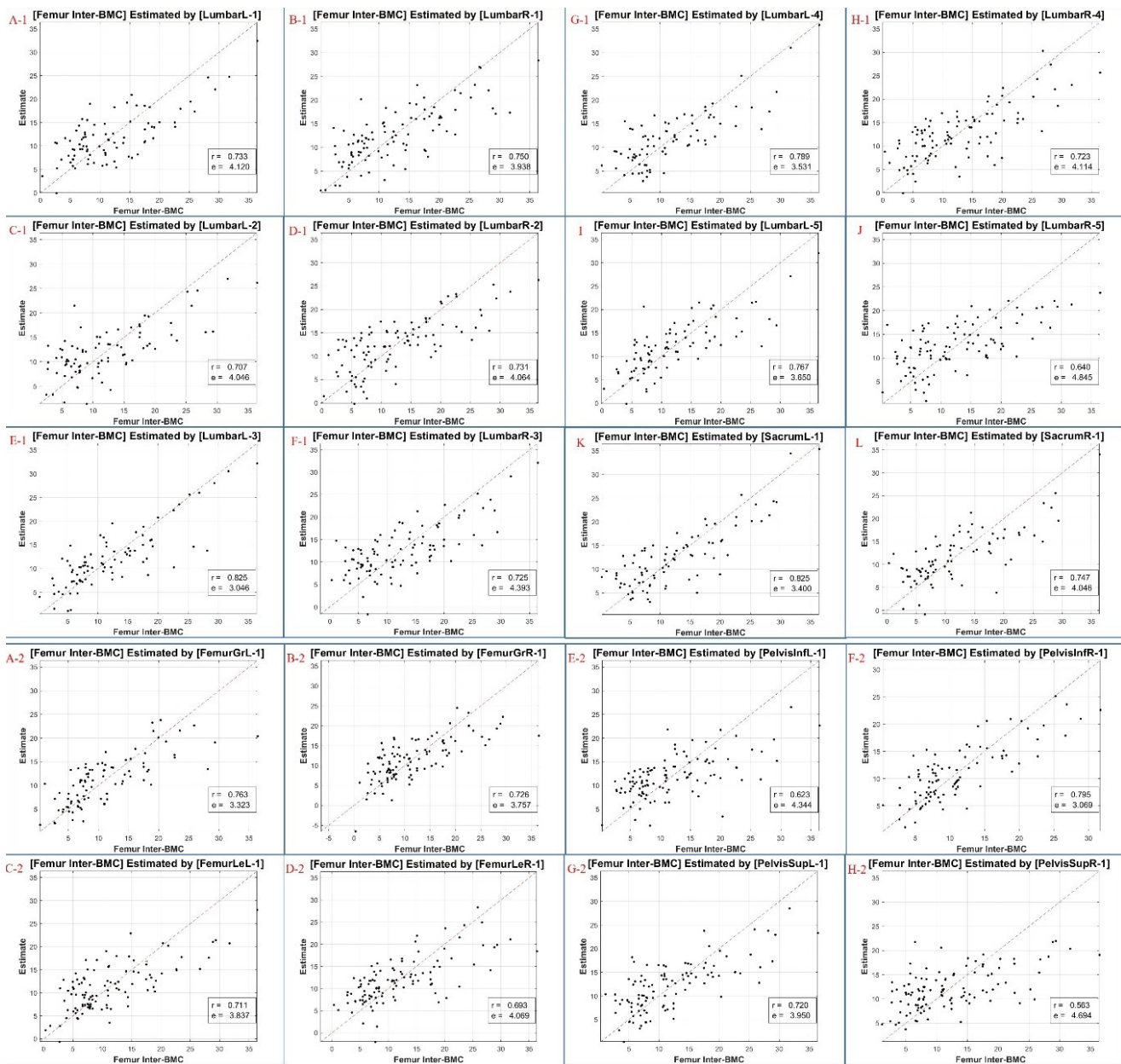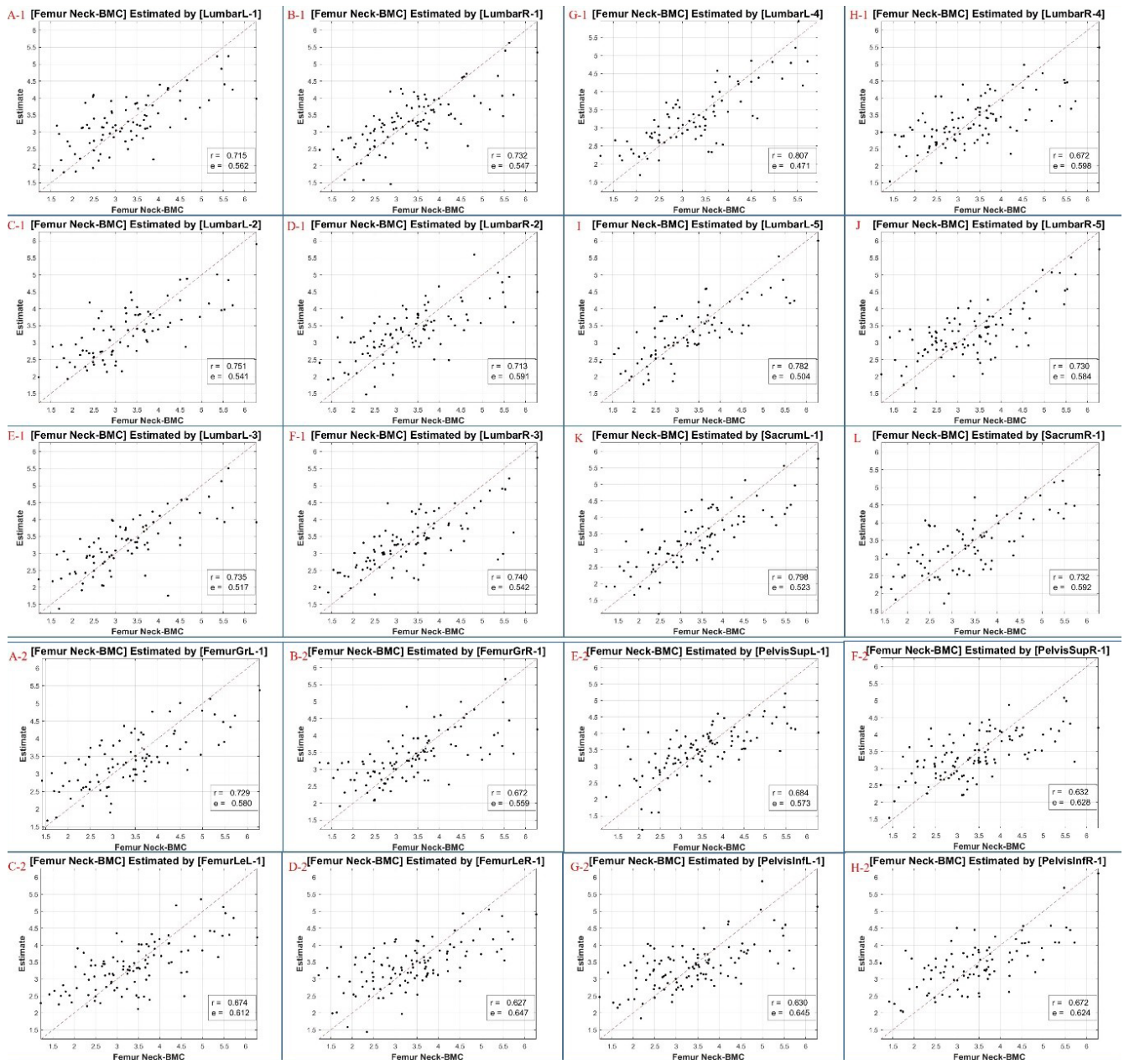

Figure S1 Scatter plots showing DXA BMC reference values for Femur Intertrochanter and corresponding estimates across cases. Circles denote their corresponding estimated values using the Linear Regression model.

Figure S2 Scatter plots displaying DXA BMD reference values for Femur Intertrochanter and the corresponding estimates across cases. Circles represent the corresponding estimated values derived from the Linear Regression model.
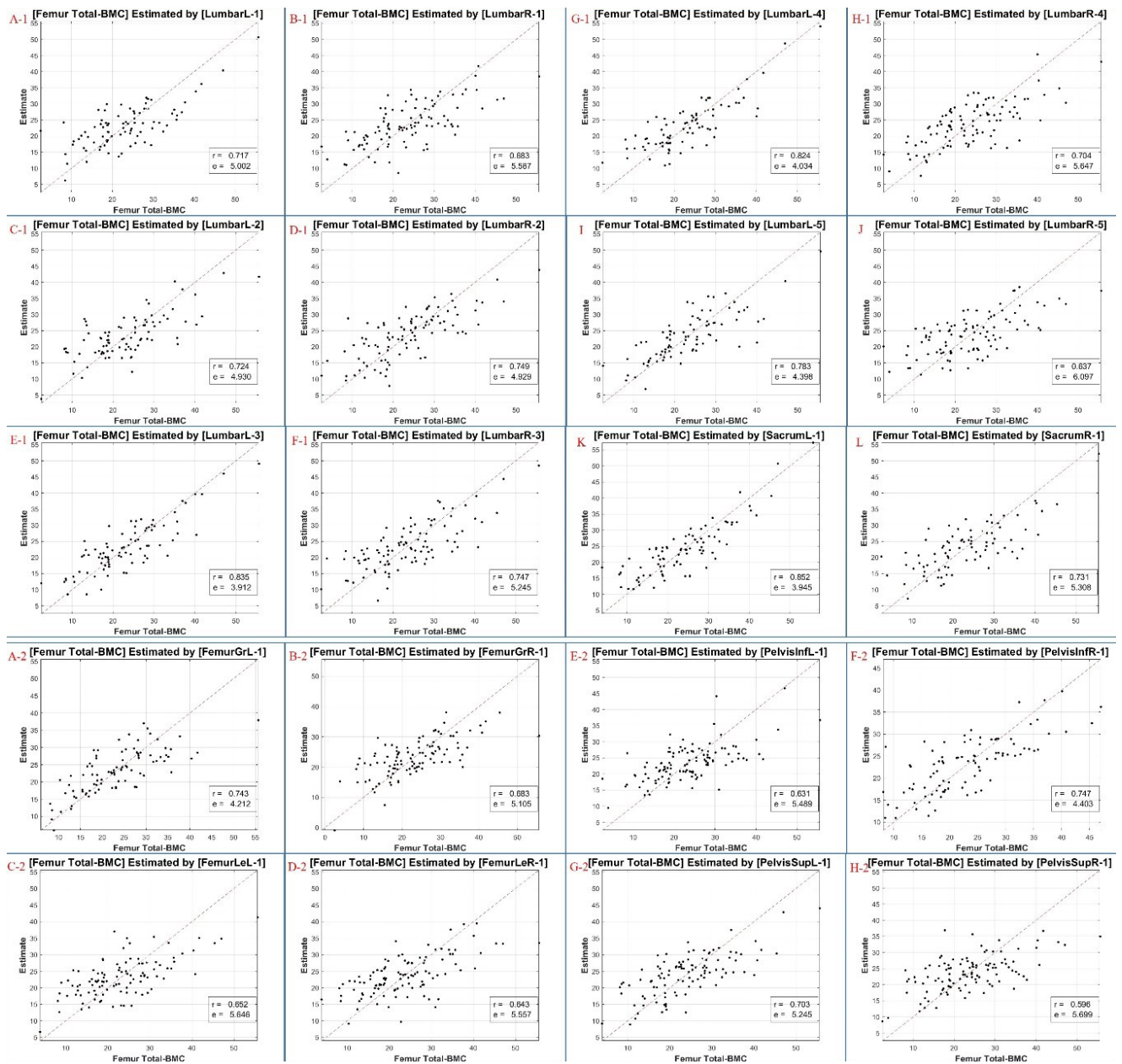
Figure S3 Scatter plots illustrating DXA BMC reference values for Femur Neck and the corresponding estimates across cases. Circles denote their corresponding estimated values obtained through the Linear Regression model.
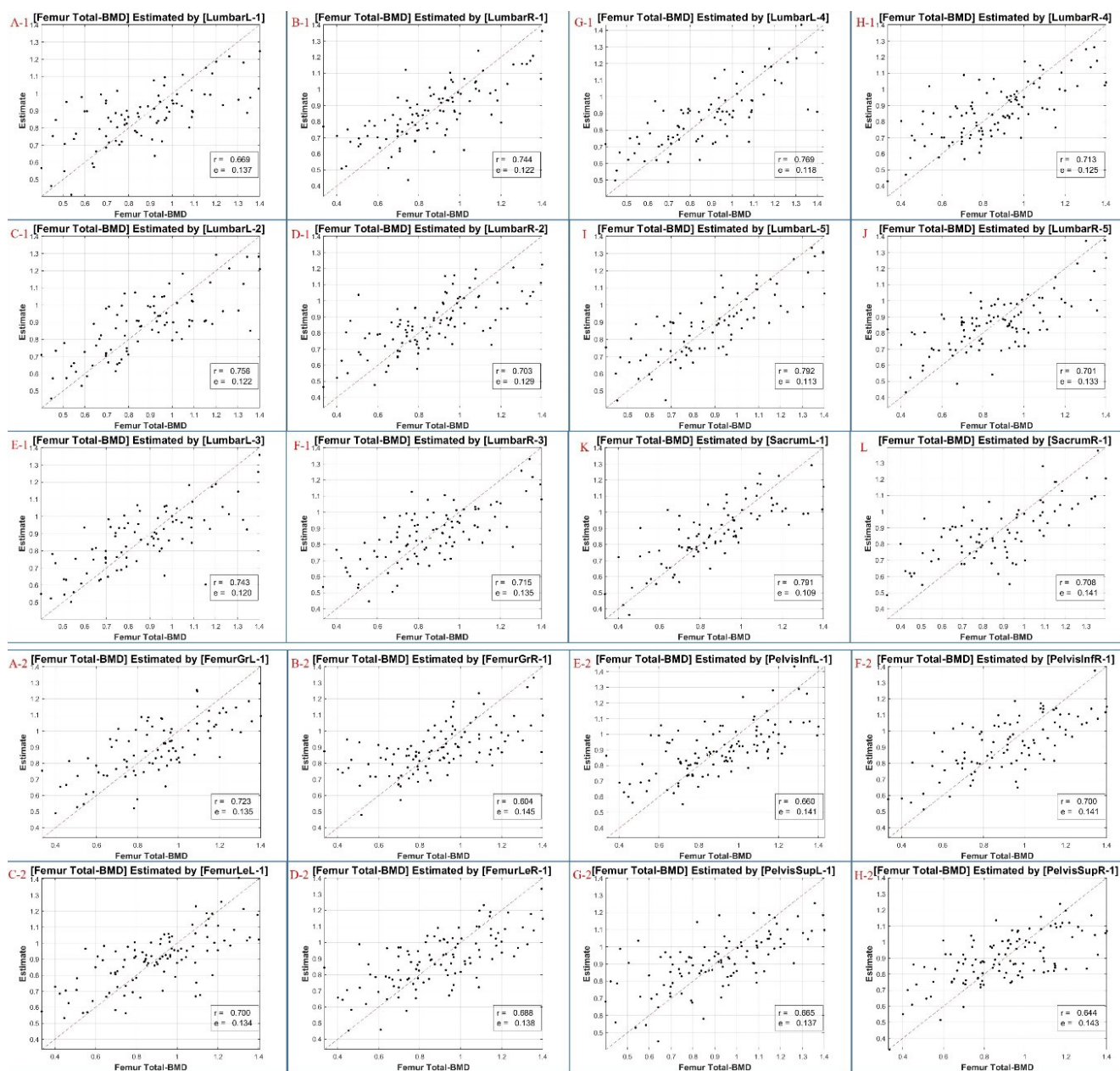
Figure S4 Scatter plots showing DXA BMD reference values for Femur Neck and corresponding estimates across cases. Circles signify their corresponding estimated values, determined by the Linear Regression model.
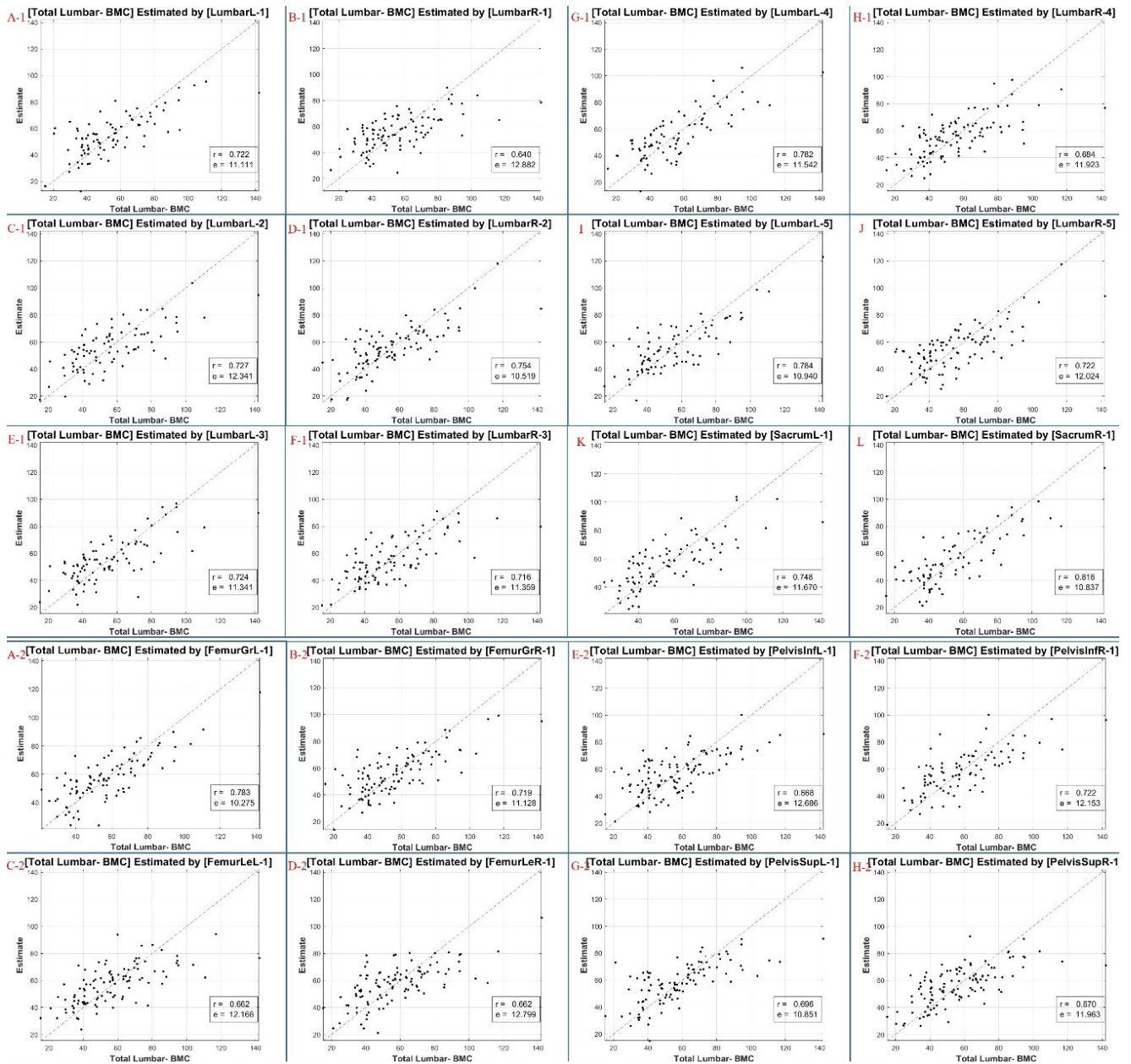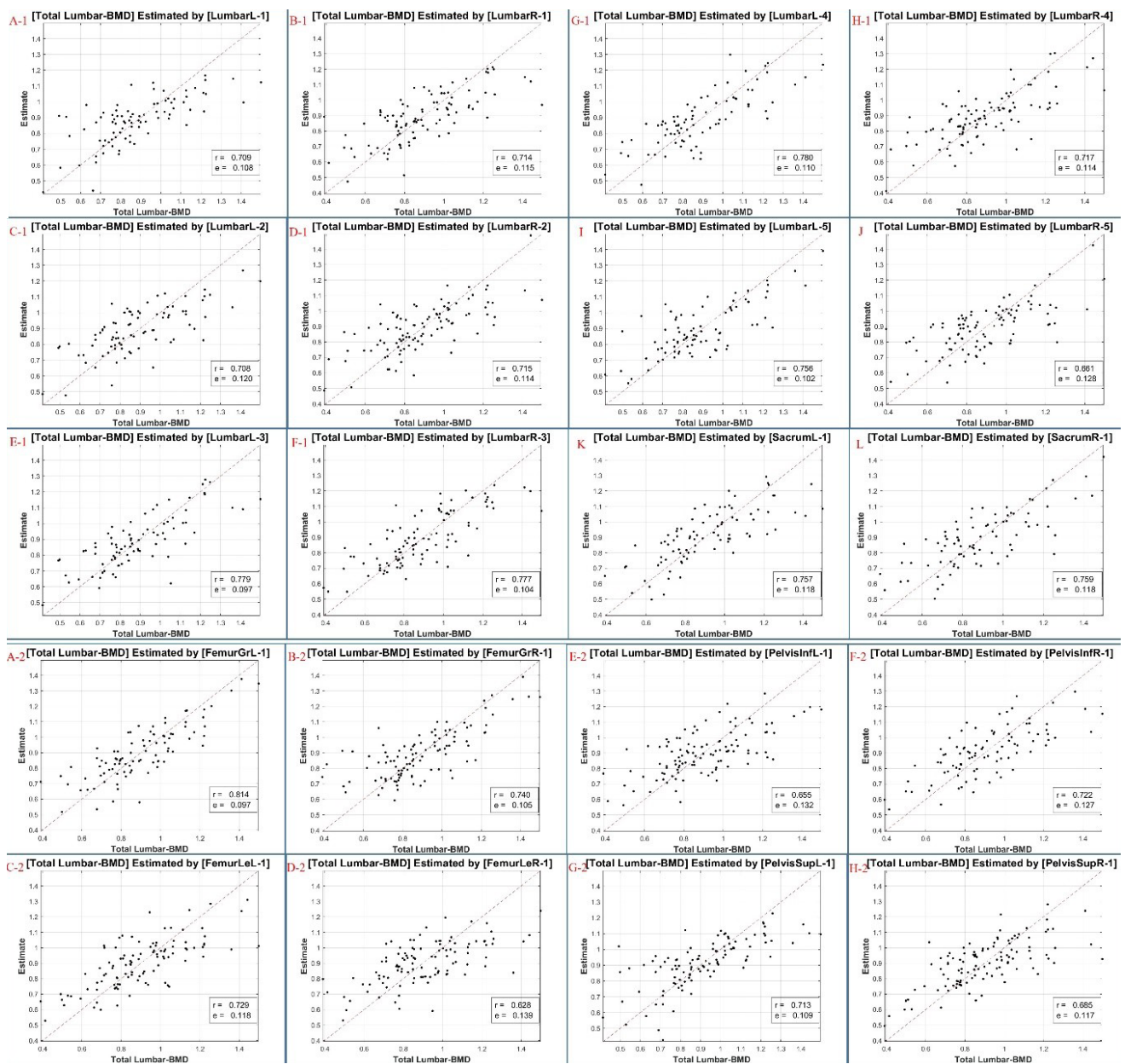
Figure S5 Scatter plots depicting DXA BMC reference values for Femur Total and corresponding estimates across cases. Circles denote their corresponding estimated values, calculated using the Linear Regression model.

Figure S6 Scatter plots illustrating DXA BMD reference values for Femur Total and the corresponding estimates across cases. Circles represent the corresponding estimated values derived from the Linear Regression model.

Figure S7 Scatter plots showing DXA BMC reference values for Total Lumbar and corresponding estimates across cases. Circles denote their corresponding estimated values, determined by the Linear Regression model.

Figure S8 Scatter plots illustrating DXA BMD reference values for Total Lumbar and the corresponding estimates across cases. Circles denote their corresponding estimated values, calculated using the Linear Regression model.